Structure–Function Mapping: Variability and *Conviction* in Tracing Retinal Nerve Fiber Bundles and Comparison to a Computational Model

Jonathan Denniss,[1,2] Andrew Turpin,[2] Fumi Tanabe,[3] Chota Matsumoto,[3] and Allison M. McKendrick[1]

[1]Optometry and Vision Sciences, The University of Melbourne, Melbourne, Australia
[2]Computing and Information Systems, The University of Melbourne, Melbourne, Australia
[3]Ophthalmology, Kinki University Faculty of Medicine, Osaka, Japan

Correspondence: Jonathan Denniss, Optometry & Vision Sciences, The University of Melbourne, Melbourne, VIC 3010, Australia; jdenniss@unimelb.edu.au.

Submitted: August 27, 2013
Accepted: December 23, 2013

Citation: Denniss J, Turpin A, Tanabe F, Matsumoto C, McKendrick AM. Structure–function mapping: variability and *conviction* in tracing retinal nerve fiber bundles and comparison to a computational model. *Invest Ophthalmol Vis Sci*. 2014;55:728–736. DOI:10.1167/iovs.13-13142

Purpose. We evaluated variability and *conviction* in tracing paths of retinal nerve fiber bundles (RNFBs) in retinal images, and compared traced paths to a computational model that produces anatomically-customized structure–function maps.

Methods. Ten retinal images were overlaid with 24-2 visual field locations. Eight clinicians and 6 naïve observers traced RNFBs from each location to the optic nerve head (ONH), recording their best estimate and *certain range* of insertion. Three clinicians and 2 naïve observers traced RNFBs in 3 images, 3 times, 7 to 19 days apart. The model predicted 10° ONH sectors relating to each location. Variability and repeatability in best estimates, *certain range* width, and differences between best estimates and model-predictions were evaluated.

Results. Median between-observer variability in best estimates was 27° (interquartile range [IQR] 20°–38°) for clinicians and 33° (IQR 22°–50°) for naïve observers. Median *certain range* width was 30° (IQR 14°–45°) for clinicians and 75° (IQR 45°–180°) for naïve observers. Median repeatability was 10° (IQR 5°–20°) for clinicians and 15° (IQR 10°–29°) for naïve observers. All measures were worse further from the ONH. Systematic differences between model predictions and best estimates were negligible; median absolute differences were 17° (IQR 9°–30°) for clinicians and 20° (IQR 10°–36°) for naïve observers. Larger departures from the model coincided with greater variability in tracing.

Conclusions. Concordance between the model and RNFB tracing was good, and greatest where tracing variability was lowest. When RNFB tracing is used for structure–function mapping, variability should be considered.

Keywords: structure–function, glaucoma, visual field, optic nerve head, mapping

In glaucoma, no single test provides complete information about a patient's disease state. Relating information from optic nerve head or retinal nerve fiber layer imaging and perimetry, therefore, is a common goal in the glaucoma literature. Relating spatially localized imaging and perimetry information typically requires the use of a structure–function map.[1–6]

The effect of localized optic nerve head damage on the visual field depends on the region of retina that is connected to the damaged optic nerve region by the axons of retinal ganglion cells. Structure–function maps in common use, therefore, have been produced by hand-tracing visible nerve fiber bundles in retinal images from superimposed perimetric test locations to the optic nerve head.[1,7,8] These maps describe a population average relationship between optic nerve head and visual field regions, but they do not take into account individual differences in ocular anatomy. Recent studies have used computational or mathematical modelling techniques to explore the potential for customizing structure–function maps to the individual patient, taking into account biometric information, such as axial length and optic nerve head position.[9–12] Maps produced by modelling techniques have been compared to hand-tracing of retinal nerve fiber bundles (RNFBs) as a reference standard against which to gauge their plausibility.[8–11,13]

There are several reasons why existing structure–function maps derived by hand-tracing of nerve fiber bundles in retinal photographs may not represent an ideal reference standard for newer maps. Tracing of RNFBs is a difficult task as bundle visibility often is poor, especially further from the optic nerve head. Since existing maps have been produced by a single observer,[7,8] the variability and repeatability of this method is unknown. Further, observers' certainty in their own tracing has not been investigated previously to our knowledge, nor has the possible influence of observers' prior clinical training.

This study had three main aims. First, we investigated between-observer variability and observers' own estimates of their certainty in tracing nerve fiber bundles from visual field locations to the optic nerve head in retinal images. Second, we investigated within-observer repeatability in the same task. Third, we compared the output from our previously published computational model[9,14] that produces anatomically-customized structure–function maps to the maps produced by the

hand-tracing method, taking into account variability and *conviction* in tracing.

Methods

This study was approved by the research ethics committees of Kinki University Faculty of Medicine and The University of Melbourne. All subjects and observers gave written informed consent to take part, and the study adhered to the tenets of the Declaration of Helsinki.

Retinal Images

Subjects for imaging (n = 32) were recruited from the Department of Ophthalmology, Kinki University, Osaka, Japan, for another study. All subjects were free from eye disease, and had clinically normal retinal and optic nerve head appearance judged by slit-lamp examination by an ophthalmologist, clear ocular media, circumpapillary retinal nerve fiber layer thickness within normal limits (Cirrus; Carl Zeiss Meditec, Dublin, CA), Snellen visual acuity 6/7.5 or better, and no history of ocular surgery. Where both eyes of a subject were eligible, one was selected at random. As part of the other study, subjects underwent retinal photography, scanning laser ophthalmoscopy (F10, 490 nm diode laser; Nidek, Gamagon, Japan) and blind spot mapping using a custom perimetric test (Octopus 900, suprathreshold Goldmann I stimulus presented on a 1° grid of dimensions 13° × 11° centered on the blind spot; Haag-Streit, Köniz, Switzerland). Throughout imaging and blind spot mapping, head position and tilt were controlled using a custom-molded face mask fixed to the chin/forehead rest of the instrument. Scanning laser ophthalmoscope images (1280 × 960 pixels, 40° × 30° field of view) were averaged using a software tracking method (RegiStax 4.0, available in the public domain at http://www.astronomie.be/registax/about.html and overlaid on the retinal photographs to create composite RNFB images. The perimetrically-mapped blind spot and fixation locations then were used to align and overlay the 24-2 visual field pattern onto the composite images (Fig. 1). Axial length also was measured (IOLMaster; Carl Zeiss Meditec).

The 32 images were ranked according to image quality (subjective focus, contrast, and alignment) by one author (JD) without reference to the anatomic data, and the best 20 images were selected for further consideration. The cutoff of 20 images, while somewhat arbitrary, enabled the few poor quality images in the dataset to be excluded without being too restrictive on the available anatomic parameters. To keep the tracing task manageable for the observers and, thus, ensure good quality data, we chose to restrict the image set further to 10 images. The optic nerve head positions relative to the fovea and axial lengths for the 20 images were plotted, and the final 10 images were selected to represent a variety of optic nerve head positions and axial lengths. None of the images featured tilted discs or extensive areas of peripapillary atrophy, and no other anatomic features (e.g., blood vessel locations) were considered in the selection of images. Demographic and anatomic information for each of the final 10 subjects is provided in Table 1. A subset of 3 images (B, C, and I) was selected randomly for the repeatability study.

Tracing of RNFBs

Images were displayed in random order on a computer monitor under standard laboratory conditions. All observers received identical written instructions on the task, to which they were free to refer at any time. The instructions included examples of RNFBs in a circular image portion (to remove context, thus, avoiding inducing prior expectation), intended to instruct the naïve observers, but provided to all. Observers traced RNFBs from each overlaid visual field location (Fig. 1) to an overlaid circle approximating the optic disc margin, recording for each their best estimate of its point of insertion with reference to the overlaid protractor. Observers also recorded the range within which they were certain that the bundle entered the optic nerve head (*certain range*), having received specific instructions that this range could be anything from 1° to 360° in width to reflect their certainty in tracing. All observers were monitored by one author (JD) during their initial attempts to ensure full comprehension of the instructions. Observers were free to vary their viewing distance and image zoom to obtain the best view, and to use the mouse cursor or another pointer to aid tracing the fibers. Observers did not mark the full course of traced axons on the images.

Observers

For the investigation of between-observer variability and observer *conviction* (see Statistical Analysis section), and the comparison to the computational model, eight clinicians and six naïve observers completed the task for all 10 images. Clinicians were experienced optometrists recruited from the Department of Optometry and Vision Sciences, The University of Melbourne, Australia, and were naïve to the computational model. Naïve observers were postgraduate students and staff of The University of Melbourne, and had no prior clinical training. None of the authors acted as observers. All observers were prepresbyopic and wore habitual refractive correction with which they had binocular Snellen visual acuity of 6/6 or better. Observers completed the task over multiple sessions, and were encouraged to take regular breaks to avoid fatigue.

To investigate repeatability of the tracing method, a further three clinicians and two naïve observers traced RNFBs in the subset of three images described above. These observers then repeated the task a further two times, with median 7 days between attempts (range, 7–19 days), without reference to their prior data.

Computational Model Relating the Visual Field to the Optic Nerve Head in Individual Eyes

Observers best estimates were compared to the output of a computational model that has been described previously.[9,14] The model produces custom maps relating any given visual field location to the optic nerve head based on the individual eye's axial length and optic nerve head position. We have shown previously the effects of these parameters on the maps produced by the model.[9] Maps were produced relating 10° optic nerve head sectors to 24-2 visual field locations using each subject's own anatomic information (Table 1).

Statistical Analysis

All analyses were carried out in the open-source statistical environment, *R*, version 2.15.0.[15] Data from left eye images were converted to right eye format where 0° was due West on the optic nerve head and sector angles increased clockwise (90° = North, 180° = East, 270° = South).

Since the insertion points of the RNFBs formed a circular domain (1° and 360° are adjacent), means of n best estimates $\alpha_1, \ldots, \alpha_n$ were calculated using the formula[16]:

$$\bar{\alpha} = a\tan 2\left(\frac{1}{n}\sum_{j=1}^{n}\sin\alpha_j, \frac{1}{n}\sum_{j=1}^{n}\cos\alpha_j\right),$$

while ranges of best estimates were the angular distance

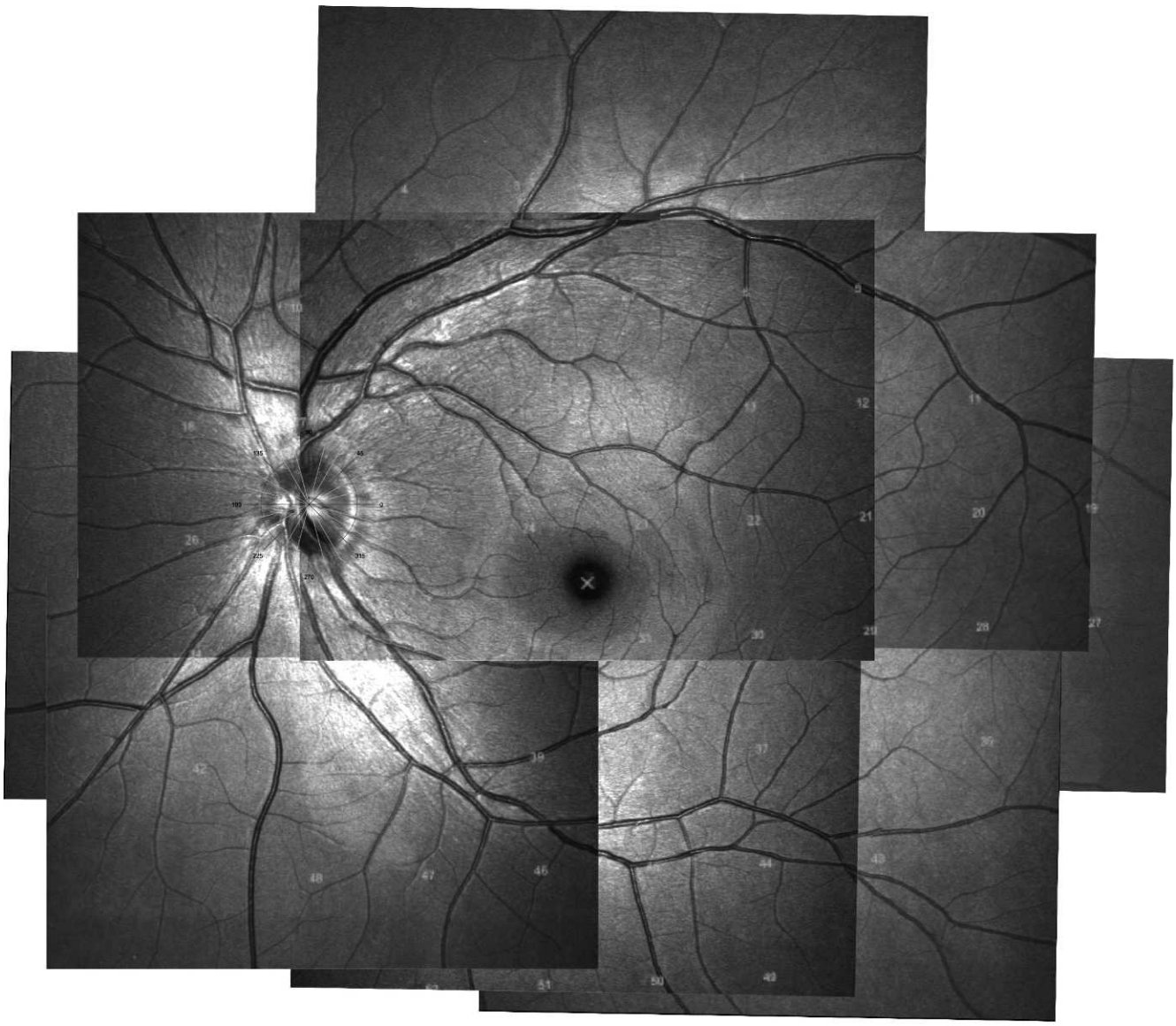

Figure 1. Example composite 490 nm scanning laser ophthalmoscope retinal image with 24-2 visual field locations overlaid according to position of perimetrically-mapped blind spot and fixation location. This image is Image I in Table 1.

Table 1. Demographic and Anatomic Information for the Final Images Selected

Image	Age, y	Sex	Eye	Axial Length, mm	Refractive Error, Spherical Equivalent, D	Blind Spot Horizontal Distance From Vertical Midline, deg	Blind Spot Vertical Distance Above Horizontal Midline, deg
A	26	F	R	24.1	+0.25	15.8	0.0
B	35	F	R	23.7	−0.25	15.7	2.2
C	35	M	L	22.2	0.00	16.1	3.0
D	61	F	L	24.4	+0.25	14.9	1.5
E	52	M	R	24.3	−1.25	16.0	2.8
F	23	F	R	26.0	−6.50	15.3	3.7
G	34	F	R	26.7	−6.75	17.1	0.8
H	31	F	R	25.3	−2.50	15.3	2.8
I	33	F	L	23.8	−0.75	15.1	4.7
J	59	M	R	22.5	0.00	16.8	1.3

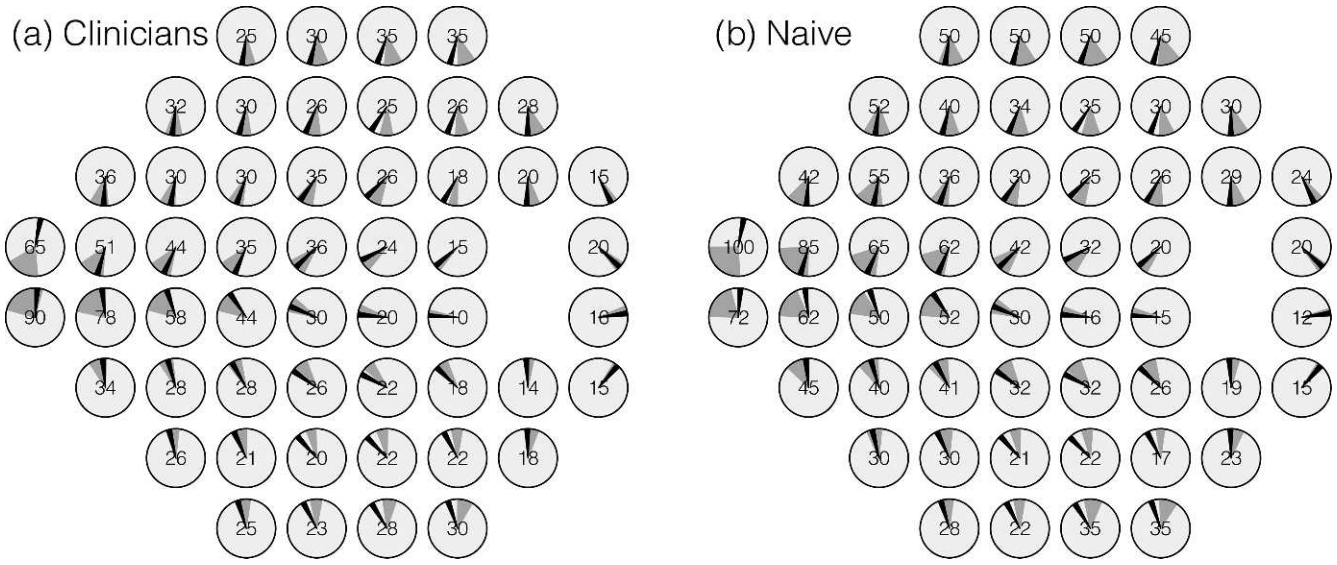

Figure 2. Between-observer variability in best estimates at each visual field location for (**a**) clinicians and (**b**) naïve observers. *Grey* shaded sectors are centered on the mean best estimate across all observers and sectors, and have width equal to the median range width of best estimates (angular distance between furthest apart best estimates) given by the group across all 10 images (also shown numerically [degrees] at each location; note that individual best estimates may fall outside of the sector shown and locations of best estimates are different for different images). *Black* shaded sectors represent the mean 10° sectors predicted by the model across all 10 images. In general superior visual field locations relate to inferior optic nerve head regions and vice versa due to the inversion of the visual field relative to the retina.

between the furthest apart best estimates. To investigate the general relationship between *certain ranges* and visual field locations across all images, independent of observer criterion and possible differences in image "difficulty," we defined *conviction* for a location L in image i as

$$conviction_L = \frac{certain\,range_L - \min\{certain\,range_i\}}{\max\{certain\,range_i\} - \min\{certain\,range_i\}} \times 100,$$

where $certain\,range_L$ is the width of the *certain range* given at location L and $\{certain\,range_i\}$ is the set of *certain range* widths given by the observer for the image. *Conviction*, therefore, can be considered the percentage certainty an observer reported for a location after normalizing for observer- and image-specific criterion (0% = minimal certainty for that image and that observer, 100% = maximal certainty for that image and that observer).

The computational model was compared to the tracing data by calculating signed and absolute angular differences between best estimates and model output, thereby evaluating systematic differences and magnitude of differences at individual locations.

The intraclass correlation coefficient (ICC)[17] was used to describe overall conformity of estimates between observers and repeatability of estimates by individual observers, with each location in each image being considered a separate target for measurement. The ICC gives the proportion of total variance in estimates across all locations in all images that is due to the targets of the estimates (the locations). Therefore, measurement error due to the observer is given by 1-ICC and a high ICC indicates good conformity or repeatability relative to the total measurement range. The ICC was calculated using the ICC() function in the *R* package psych[18] according to the ICC(2,1) and ICC(3,1) methods described by Shrout and Fleiss[17] for conformity between observers and repeatability by individual observers, respectively. The Nest() function in the *R* package ICC[19] showed that 3 repeats of 3 images per observer were sufficient to yield an ICC with 95% confidence interval (CI) width < 0.1 when ICC > 0.79 in the repeatability study. The same function showed that with 6 or 8 observers per group and 10 images, ICC for conformity within groups would have 95% CI width < 0.1 irrespective of ICC.

Results

Observers from both groups took a median of 20 minutes per image (interquartile range [IQR] 15–27 minutes for clinicians and 15–25 minutes for naïve observers) to trace the RNFBs.

Variability in Tracing RNFBs

Across all locations of all images, ICC for conformity between observers was 0.97 (95% CI 0.97–0.98) within the clinician group, and 0.89 (95% CI 0.88–0.90) within the naïve group. These values suggested good conformity between observers, but must be contextualized by the absolute between-observer variability in best estimates, which varied across visual field locations, generally being greater at locations further from the optic nerve head (Fig. 2). Median range of best estimates (median angular distance between furthest apart best estimates across the 10 images) for a visual field location was 27° (IQR 20°–38°) for clinicians and 33° (IQR 22°–50°) for naïve observers. Spearman's rank correlation between median range of best estimates and distance from the optic nerve head was 0.72 for clinicians and 0.73 for naïve observers (both $P < 0.001$).

Conviction in Tracing RNFBs

Observers' median *conviction* in tracing RNFBs from each visual field location is shown in Figure 3 as the size of the circles at each location. The median widths of raw *certain ranges* also are shown for each location. It is apparent that *conviction* decreases further from the optic nerve head, more so for the naïve observers than the clinicians. Raw *certain range* widths were substantially wider for naïve observers

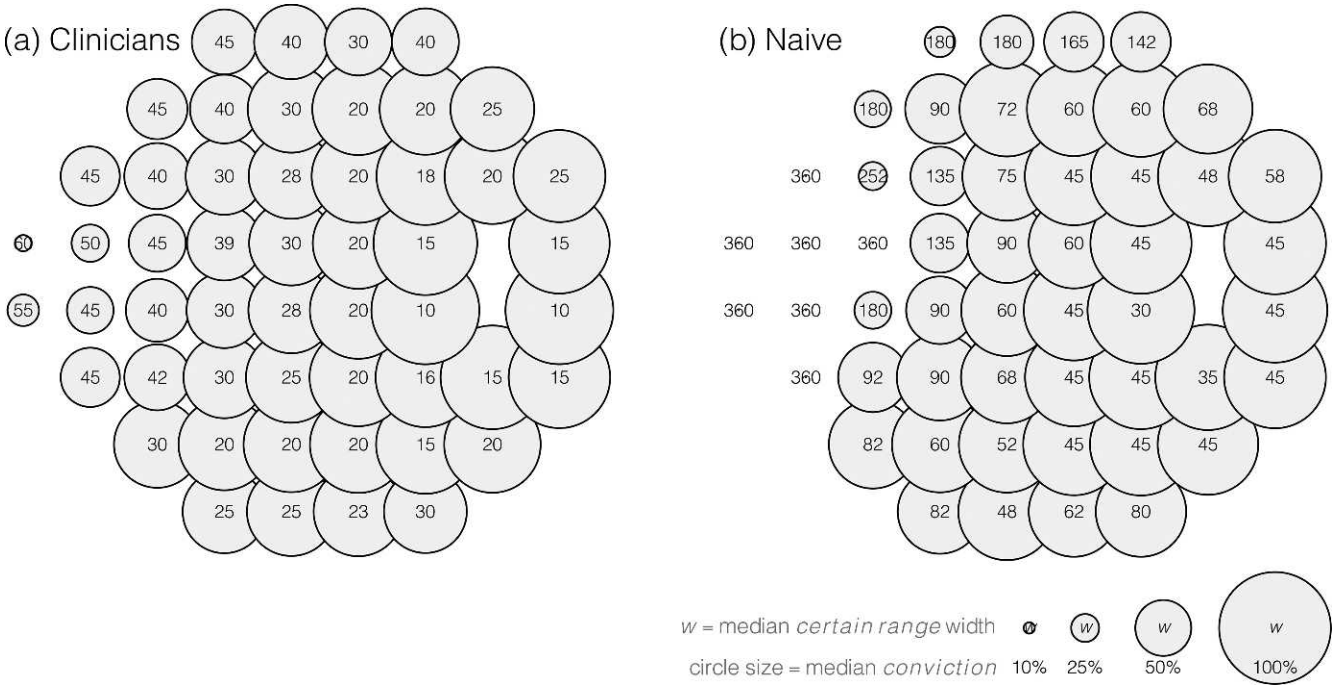

Figure 3. *Conviction* in tracing RNFBs from each visual field location for (**a**) clinicians and (**b**) naïve observers. *Circle* size is proportional to median *conviction* of all observers across all images. Median raw *certain range* width (degrees) is given numerically at each location.

(median 75°, IQR 45°–180°) than for clinicians (median 30°, IQR 14°–45°, Mann-Whitney U test $P < 0.001$). Spearman's rank correlation between median *conviction* and distance from the optic nerve head was –0.85 for clinicians and –0.82 for naïve observers (both $P < 0.001$, negative coefficient indicates decreasing *conviction* with increasing distance from the optic nerve head).

Repeatability of Tracing RNFBs

Table 2 shows ICC for repeatability of best estimates across all locations of all images by each observer in the repeatability study. The values indicate good within-observer repeatability, but must be considered in the context of absolute repeatability, shown for each visual field location in Figure 4. The median range of best estimate repeats (median angular distance between furthest apart best estimates by individual observers) for a visual field location was 10° (IQR 5°–20°) for clinicians and 15° (IQR 10°–29°) for naïve observers. Similar to between-observer variability and *conviction*, repeatability generally was better close to the optic nerve head (Fig. 4). Spearman's rank correlation between median range of best estimate repeats and distance from the optic nerve head across visual field locations was 0.64 for clinicians and 0.51 for naïve observers (both $P < 0.001$).

Table 2. The ICCs for Repeatability of Best Estimates by Each Observer in the Repeatability Study

Observer	ICC	95% CI
Clinician 1	0.95	0.94–0.97
Clinician 2	0.90	0.87–0.92
Clinician 3	0.97	0.96–0.97
Naïve observer 1	0.95	0.94–0.96
Naïve observer 2	0.82	0.78–0.86

Comparison Between Computational Model and Tracing of RNFBs

Mean model-predicted sectors at each visual field location are shown in Figure 2. Across all locations of all images, centers of model-predicted sectors were median 2° anticlockwise of clinicians' best estimates (IQR 19° anticlockwise to 16° clockwise), and median 2° anticlockwise of naïve observers' best estimates (IQR 22° anticlockwise to 18° clockwise). These results indicate negligible overall systematic differences between the model and best estimates, but do not adequately describe the magnitude of likely difference between the model and best estimates at a single location, for which we next consider absolute differences. Across all locations of all images, absolute differences between centers of model-predicted sectors and best estimates were median 17° (IQR 9°–30°) for clinicians, and median 20° (IQR 10°–36°) for naïve observers.

Figure 5 shows how signed (Figs. 5a, 5b) and absolute (Figs. 5c, 5d) differences between best estimates and model predictions related to between-observer variability in best estimates and observers' *conviction* in tracing across visual field locations. Locations with greater discordance between the model and observers' best estimates tended to be those with lower observer *conviction* and greater between-observer variability in best estimates. Spearman's rank correlation between median range of best estimates and median *conviction* was –0.91 for clinicians and –0.93 for naïve observers (both $P < 0.001$). Spearman's rank correlation between median *conviction* and absolute differences between best estimates and model predictions was –0.35 for clinicians and –0.36 for naïve observers (both $P = 0.01$). Spearman's correlation between median range of best estimates, and absolute differences between best estimates and model predictions was 0.42 ($P = 0.002$) for clinicians and 0.47 ($P < 0.001$) for naïve observers. For locations with larger differences between model-predicted sectors and observers' best estimates, the tendency was for best estimates to be more nasal on the optic nerve head than the model-predicted sectors (Figs.

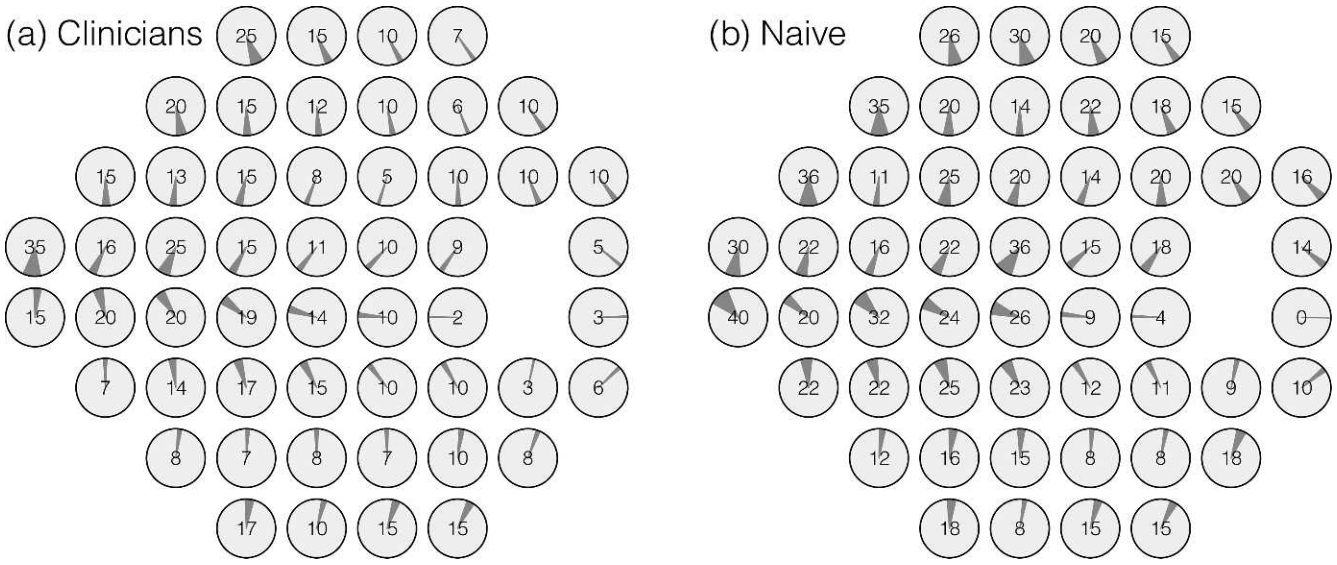

Figure 4. Range of best estimate repeats at each visual field location in the repeatability study for (**a**) clinicians and (**b**) naïve observers. *Grey* shaded sectors are centered on the mean best estimate given by observers across their three repeats of three images. The width of the sectors represents the median range of best estimate repeats (also shown numerically [degrees] at each location; note that individual best estimates may fall outside of the sector shown).

5a, 5b). This also can been seen in the most superior and most inferior locations in Figure 2. The six visual field locations closest to the papillomacular bundle (i.e., the four locations around fixation and the two locations immediately nasal to the blind spot) are marked with an "X" in Figure 5. These locations exhibited close agreement between the model-predicted sectors and observers best estimates, and observers showed high *conviction* and low variability in best estimates at these locations. Several outliers in Figure 5 are marked with their visual field coordinates, and share common properties of large distance from the optic nerve head, high between-observer variability in best estimates, and low observer *conviction* in tracing. In Figures 5c and 5d, most points lie beneath the line of equality, indicating that the magnitude of differences between the model and best estimates typically was less than the magnitude of between-observer variability in best estimates.

Discussion

On average, between-observer variability in tracing RNFBs in this study was 27° to 30°. Much greater variability was apparent at the 24-2 visual field locations furthest from the optic nerve head, while variability at points close to the optic nerve head was lower. The range of within-observer repeatability generally was less than that of between-observer variability, 10° to 15°. Both observer *conviction* and within-observer repeatability followed a similar pattern across the 24-2 visual field locations studied to between-observer variability, being better close to the optic nerve head, and worse at more distant locations. While this is the first formal report of variability, *conviction*, and repeatability in tracing RNFBs in images to our knowledge, the observed pattern across the visual field is somewhat unsurprising. It can be seen readily in retinal images (e.g., Fig. 1) that the visibility of RNFBs is much greater close to the optic nerve head, and declines substantially further away. This pattern further is consistent with the findings of Garway-Heath et al.[7] and Lamparter et al.,[11] who were able to trace fibers from central and arcuate locations to the optic nerve head in more of their images than they could for more peripheral locations.

The inherent variability in tracing of RNFBs shown in this study should be taken into account in future studies using this method to create, or as a reference standard for, structure–function maps. These findings also have important implications for the use of existing structure–function maps in clinical practice. Clinicians should be mindful that these maps represent population average relationships between the optic nerve head and visual field, and, therefore, may not accurately reflect this relationship in individual patients whose ocular anatomy may differ. Further, the variability in the hand-tracing method used to create the maps in common clinical use[1,7] means that they may contain inaccuracies, particularly further from the optic nerve head. These inaccuracies and variations with anatomy may not be clinically important in some cases as the optic nerve head typically is divided into large sectors, meaning that the variation may be within a sector. However, it is likely that in many cases, individual variations in anatomy and unaccounted for variability in the methods used to create structure–function maps may result in visual field locations being mapped to entirely different optic nerve head sectors than they truly relate to. These errors in structure–function mapping potentially reduce the concordance between information available to clinicians from structural and functional tests, reducing certainty in diagnosis of disease or disease progression.

Concordance between the computational model and observers' best estimates generally was good with differences between the two being largest where variability and *conviction* in tracing were worst. Overall systematic differences between the model and best estimates were negligible, but the magnitude of differences at individual locations was larger, being on average 17° to 20°. These differences were, however, typically smaller than the between-observer variability in best estimates (Figs. 5c, 5d). Notably, concordance between observers' best estimates and the computational model was strong at the visual field locations in the region of the papillomacular bundle (Fig. 5), an area also of good *conviction* and low variability in tracing. In this region the model typically predicts that RNFBs take a direct course to the nearest point of

Investigative Ophthalmology & Visual Science

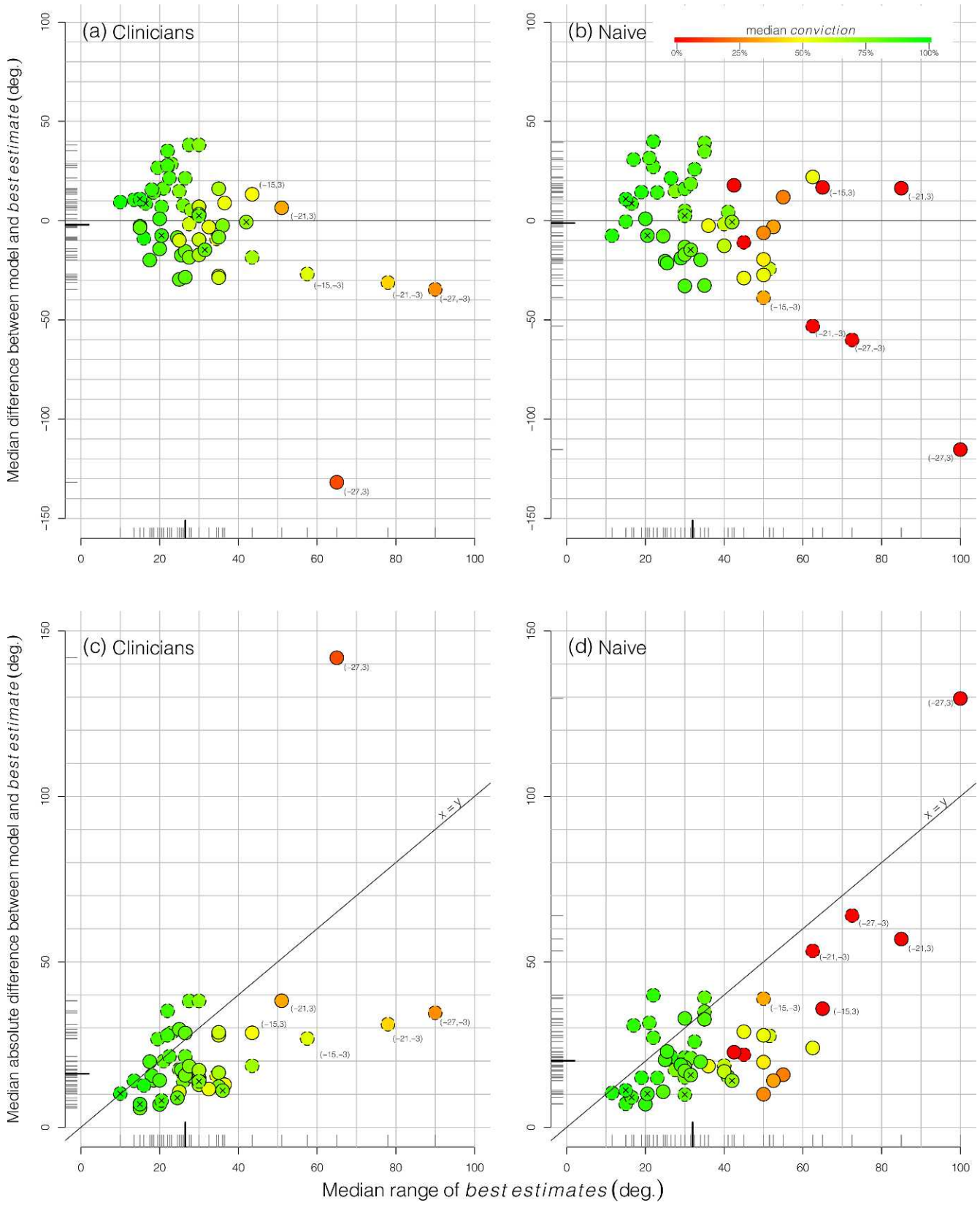

Figure 5. Median between-observer variability in tracing RNFBs versus median difference (*upper panels*) and median absolute difference (*lower panels*) between the computational model and observers' best estimates for (**a**, **c**) clinicians and (**b**, **d**) naïve observers. Each point represents a 24-2 visual field location ($n = 52$), median observer *conviction* in tracing is represented by the *color* of each point. *Circles* with *dashed borders* represent inferior visual field locations, *circles* with *solid borders* represent superior visual field locations. Points marked with an "X" indicate the six visual field locations immediately nasal to the blind spot and closest to the papillomacular bundle. In the *upper panels*, positive differences (*y*-axis) indicate that best estimates were clockwise of model-predicted sectors. The *grey tick marks* on the axes show the distributions of the variables, and

the *longer black tick marks* show the medians. Coordinates adjacent to outlying points give the 24-2 visual field locations in degrees of visual angle. The *diagonal lines* in the *lower panels* are lines of equality ($x = y$), where median variability in tracing is equal to median absolute difference between tracing and the model.

the optic nerve head, such that their insertion point reflects the fovea-optic nerve head axis. Our sample included a range of optic nerve head positions above the horizontal midline (from 0°–4.7°, Table 1), and we have shown previously that this vertical positioning of the optic nerve head is the main contributor to the considerable anatomic variation in model predictions in these locations,[9] which is validated somewhat by the current findings.

One regular pattern of discordance observed was that model predictions tended to predict more temporal insertion of RNFBs to the optic nerve head than did observers' best estimates from some arcuate locations (Figs. 2, 5a, 5b) where *conviction* and variability were reasonable, and bundles are clearly visible in Figure 1. It should be remembered that the retinal nerve fiber layer is a three-dimensional structure; in retinal images we are only able to view the most prominent, superficial nerve fiber bundles. The RNFBs originating from more peripheral retina typically traverse the retina more vitreally than do bundles originating closer to the optic nerve head,[20] before passively intermingling in the peripapillary region as fiber bundles converge on the optic nerve head.[20–23] We note in passing that much of the apparent controversy in the cited literature surrounding the organization of RNFBs in the z-plane of the nerve fiber layer may be due to measurement in the peripapillary area where intermingling occurs,[20] or study of animal retinae that have major anatomic differences to humans.[24] Given the more superficial location of more peripherally-originating nerve fiber bundles, and the larger diameter of more peripheral retinal ganglion cell axons,[25,26] it is likely that the nerve fiber bundles visible to observers in the present images at these arcuate locations actually are more peripherally-originating bundles overlaying those really of interest. Since more peripheral bundles tend to be nasally displaced on the optic nerve head, this may explain the apparent discordance between the model and observers' best estimates. A clinical study supports this hypothesis, showing an apparently straighter course of deeper arcuate fiber bundles in patients with superficial nerve fiber layer defects due to glaucoma.[27]

One visual field location (–27, 3) appears as a notable outlier in Figure 5. The model predicts that on average in the study population this location corresponds to the superior optic nerve head (Fig. 2) while convention would relate it to the inferior optic nerve head. We have described previously in detail why this may be the case.[9] Briefly, the model assumes that retinal ganglion cell axons initially take the shortest path from their retinal origin toward the optic nerve head. They then are diverted by the fovea and other axons originating closer to the optic nerve head, moving their final insertion point at the optic nerve head nasally. The (–27, 3) visual field location ([–27, –3] retinal location), while inferior to the horizontal midline of the retina, can be superior to the great circle through the optic nerve head and fovea when the optic nerve head itself is superior to the horizontal midline of the retina, as occurs commonly in our data and that of others.[7,11] Under these circumstances, the axons' shortest path to the optic nerve head takes it to the superior side of the optic nerve head. It should be noted that this location is the furthest from the optic nerve head, has large between-observer variability in best estimates, and very low observer *conviction* in tracing. Therefore, this study does not tell us whether this model prediction is correct or not.

The effect of prior clinical training on tracing of RNFBs has not been investigated previously to our knowledge. While best estimates were similar between clinicians and naïve observers, clinicians' best estimates were less variable, and clinicians reported greater certainty in tracing. It is possible that these results reflect a preconception of a certain pattern in the clinicians that they revert to when nerve fiber bundles are not easily visible in the image. A similar general pattern also probably would be learned by the naïve observers during the task, though they may be less certain of it. That within-observer repeatability was better than between-observer variability further suggested an effect of prior knowledge, which may explain the repeatability at the most peripheral locations (Fig. 4), which is considerably better than might be expected from the variability and *conviction* at these locations.

Due to the limitations of RNFB tracing demonstrated herein, further validation of the computational model will require the combination of evidence from different approaches. Detailed histologic or autoradiographic studies, preserving the anatomy of individual eyes would be useful. Further studies correlating regions of structural and functional damage in optic neuropathies,[14,28–30] taking account of individual biometry data, also are warranted. More objective in vivo tracing of RNFBs by automated software[31] may soon be enabled by high-resolution adaptive optics imaging of the retinal nerve fiber layer,[32–34] eliminating many of the limitations of hand-tracing. It is an advantage of the computational modelling approach to structure–function mapping that the model may be modified as suggested by new evidence becoming available.[9]

The images used in this study were composites of scanning laser ophthalmoscope images. Due to warping in the images, there were some small misalignments in the composite images (Fig. 1) that were not correctable. It is possible that these misalignments might affect observers' best estimates; however, the misalignments were small and appeared to be accounted for easily by the observers. Informal testing by the authors suggested that any variability induced by these misalignments was much smaller than the total variability reported, and anecdotally our observers reported that they did not have difficulty tracing across the misalignments. Due to practical limitations on the time observers could reasonably spend on the tracing task while providing reliable data, the tracing of nerve fiber bundles in this study was limited to 24-2 visual field locations and to a sample of 10 images. The 24-2 locations were chosen to represent the most commonly studied area of the visual field in glaucoma, though the computational model can be used to construct structure–function maps for any central retinal locations.[9,14] The 10 images used were deliberately selected to represent a variety of optic nerve head positions and axial lengths, to test the computational model across a variety of parameters. However, it is, of course, possible that the findings of this study may not generalize to other anatomies that fall outside of the range tested. Examples of such anatomies include (uncommon) cases where the optic nerve head is below the horizontal midline, and cases of high refractive error where the assumptions of the model may be violated by unusual eye shape.

In conclusion, tracing of nerve fiber bundles in retinal images produces variable results between-observers, particularly further from the optic nerve head. This variability should be taken into account when using this method to create, or as a reference for, structure–function maps. The computational model[9,14] showed good concordance with maps produced by

hand-tracing, notwithstanding the demonstrated limitations of the tracing method as a reference standard.

Acknowledgments

Presented in part at the annual meeting of the Association for Research in Vision and Ophthalmology, Seattle, Washington, May 5–9, 2013.

Supported by Australian Research Council Linkage Project LP100100250 (with Heidelberg Engineering GmbH, Heidelberg, Germany), Australian Research Council Future Fellowship FT0990930 (AMM), Australian Research Council Future Fellowship FT0991326 (AT), and The University of Melbourne K.M. Brutton Bequest (JD). The authors alone are responsible for the content and writing of the paper.

Disclosure: **J. Denniss**, Heidelberg Engineering GmbH (F); **A. Turpin**, Heidelberg Engineering GmbH (F); **F. Tanabe**, None; **C. Matsumoto**, None; **A.M. McKendrick**, Heidelberg Engineering GmbH (F)

References

1. Garway-Heath DF, Holder GE, Fitzke FW, Hitchings RA. Relationship between electrophysiological, psychophysical, and anatomical measurements in glaucoma. *Invest Ophthalmol Vis Sci*. 2002;43:2213–2220.
2. Harwerth RS, Wheat JL, Fredette MJ, Anderson DR. Linking structure and function in glaucoma. *Prog Retin Eye Res*. 2010; 29:249–271.
3. Hood DC, Kardon RH. A framework for comparing structural and functional measures of glaucomatous damage. *Prog Retin Eye Res*. 2007;26:688–710.
4. Boland M, Quigley HA. Evaluation of a combined index of optic nerve structure and function for glaucoma diagnosis. *BMC Ophthalmol*. 2011;11:6.
5. Denniss J, McKendrick AM, Turpin A. Towards patient-tailored perimetry: automated perimetry can be improved by seeding procedures with patient-specific structural information. *Trans Vis Sci Tech*. 2013;2:3.
6. Denniss J, Schiessl I, Nourrit V, Fenerty CH, Gautam R, Henson DB. Relationships between visual field sensitivity and spectral absorption properties of the neuroretinal rim in glaucoma by multispectral imaging. *Invest Ophthalmol Vis Sci*. 2011;52: 8732–8738.
7. Garway-Heath DF, Poinoosawmy D, Fitzke FW, Hitchings RA. Mapping the visual field to the optic disc in normal tension glaucoma eyes. *Ophthalmology*. 2000;107:1809–1815.
8. Jansonius NM, Nevalainen J, Selig B, et al. A mathematical description of nerve fiber bundle trajectories and their variability in the human retina. *Vision Res*. 2009;49:2157–2163.
9. Denniss J, McKendrick AM, Turpin A. An anatomically customizable computational model relating the visual field to the optic nerve head in individual eyes. *Invest Ophthalmol Vis Sci*. 2012;53:6981–6990.
10. Jansonius NM, Schiefer J, Nevalainen J, Paetzold J, Schiefer U. A mathematical model for describing the retinal nerve fiber bundle trajectories in the human eye: average course, variability, and influence of refraction, optic disc size and optic disc position. *Exp Eye Res*. 2012;105:70–78.
11. Lamparter J, Russell RA, Zhu H, et al. The influence of inter-subject variability in ocular anatomical variables on the mapping of retinal locations to the retinal nerve fibre layer and optic nerve head. *Invest Ophthalmol Vis Sci*. 2013;54: 6074–6082.
12. Carreras FJ, Rica R, Delgado AV. Modeling the patterns of visual field loss in glaucoma. *Optom Vis Sci*. 2011;88:E63–E79.
13. Airaksinen PJ, Doro S, Veijola J. Conformal geometry of the retinal nerve fiber layer. *PNAS*. 2008;105:19690–19695.
14. Turpin A, Sampson GP, McKendrick AM. Combining ganglion cell topology and data of patients with glaucoma to determine a structure–function map. *Invest Ophthalmol Vis Sci*. 2009;50: 3249–3256.
15. R Development Core Team. *R: A Language and Environment for Statistical Computing*. Vienna, Austria: R Foundation for Statistical Computing; 2012. Available at: http://www.R-project.org/, accessed July 10, 2013.
16. Rao Jammalamadaka S, SenGupta A. *Topics in Circular Statistics*. Singapore: World Scientific; 2001.
17. Shrout PE, Fleiss JL. Intraclass correlations: uses in assessing rater reliability. *Psychol Bull*. 1979;86:420–428.
18. Revelle W. Procedures for Personality and Psychological Research. Evanston, IL: Northwestern University; 2013. Available at: http://cran.r-project.org/web/packages/psych/index.html. Accessed July 10, 2013.
19. Wolak ME, Fairbairn DJ, Paulsen YR. Guidelines for estimating repeatability. *Methods Ecol Evol*. 2012;3:129–137.
20. Ogden TE. Nerve fiber layer of the macaque retina: retinotopic organization. *Invest Ophthalmol Vis Sci*. 1983;24:85–98.
21. Radius RL, Anderson DR. The course of axons through the retina and optic nerve head. *Arch Ophthalmol*. 1979;97:1154–1158.
22. Minckler DS. The organization of nerve fiber bundles in the primate optic nerve head. *Arch Ophthalmol*. 1980;98:1630–1636.
23. Fitzgibbon T, Taylor SF. Retinotopy of the human retinal nerve fibre layer and optic nerve head. *J Comp Neurol*. 1996;375: 238–251.
24. Ogden TE. Nerve fiber layer of the owl monkey retina: retinotopic organization. *Invest Ophthalmol Vis Sci*. 1983;24: 265–269.
25. Fitzgibbon T, Funke K, Eysel UT. Anatomical correlations between soma size, axon diameter, and intraretinal length for the alpha ganglion cells of the cat retina. *Vis Neurosci*. 1991;6: 159–174.
26. Walsh N, Fitzgibbon T, Ghosh KK. Intraretinal axon diameter: a single cell analysis in the marmoset (Callithrix jacchus). *J Neurocytol*. 1999;28:989–998.
27. Jeoung JW, Kim TW, Kang KB, Lee JJ, Park KH, Kim DM. Overlapping of retinal nerve fibers in the horizontal plane. *Invest Ophthalmol Vis Sci*. 2008;49:1753–1757.
28. Anton A, Yamagishi N, Zangwill L, Sample PA, Weinreb RN. Mapping structural to functional damage in glaucoma with standard automated perimetry and confocal scanning laser ophthalmoscopy. *Am J Ophthalmol*. 1998;125:436–446.
29. Gardiner SK, Johnson CA, Cioffi GA. Evaluation of the structure–function relationship in glaucoma. *Invest Ophthalmol Vis Sci*. 2005;46:3712–3717.
30. Ferreras A, Pablo LE, Garway-Heath DF, Fogagnolo P, Garcia-Feijoo J. Mapping standard automated perimetry to the peripapillary retinal nerve fiber layer in glaucoma. *Invest Ophthalmol Vis Sci*. 2008;49:3018–3025.
31. Richards DW, Janesick JR, Elliot ST, et al. Enhanced detection of normal retinal nerve-fiber striations using a charge-coupled device and digital filtering. *Graefes Arch Clin Exp Ophthalmol*. 1993;231:595–599.
32. Huang G, Qi X, Chui TYP, Zhong Z, Burns SA. A clinical planning module for adaptive optics SLO imaging. *Optom Vis Sci*. 2012;89:593–601.
33. Takayama K, Ooto S, Hangai M, et al. High-resolution imaging of the retinal nerve fiber layer in normal eyes using adaptive optics scanning laser ophthalmoscopy. *PLoS One*. 2012;73: e33158.
34. Takayama K, Ooto S, Hangai M, et al. High-resolution imaging of retinal nerve fiber bundles in glaucoma using adaptive optics scanning laser ophthalmoscopy. *Am J Ophthalmol*. 2013;155:870–881.

Investigative Ophthalmology & Visual Science